

Table 1
The Binning of the 4FGL Fit

Source Class	Variable	Min	Max	Number of Bins	Scaling
ALL	S [$\text{cm}^{-2} \text{s}^{-1}$]	10^{-10}	10^{-7}	10	log
	Γ	1.0	3.5	1	linear
BLZ	S [$\text{cm}^{-2} \text{s}^{-1}$]	10^{-10}	10^{-7}	10	log
	Γ	1.0	3.5	1	linear
	z	0.0	4.0	6	log in $(1+z)$
BLL	S [$\text{cm}^{-2} \text{s}^{-1}$]	10^{-10}	10^{-7}	10	log
	Γ	1.6	2.4	5	linear
	z	0.0	4.0	6	log in $(1+z)$
FSRQ	S [$\text{cm}^{-2} \text{s}^{-1}$]	10^{-10}	10^{-7}	10	log
	Γ	2.1	2.9	5	linear
	z	0.0	4.0	6	log in $(1+z)$

However, our models are allowed to lie above the observed source count distribution, because of unassociated sources. In this sense, the BLZ provides a lower bound for our models (labeled χ_{BLZ}^2).

- Our BLL model has to explain at least the observed source count distribution of BLLs, and thus also provides a lower bound (labeled χ_{BLL}^2).
- In analogy to BLL, the FSRQ model also receives a lower bound from the observed source count distribution (labeled χ_{FSRQ}^2).

Each of these constraints would give rise to a contribution to the 4FGL χ^2 . However, a naive sum of the χ^2 from the three lower bounds would lead to double counting, since the BLL and FSRQ sources also appear in the BLZ class. To avoid this, we consider only the most constraining lower bound between the BLZ case and the combination of BLLs and FSRQs, i.e.:

$$\chi_{\text{4FGL}}^2 = \chi_{\text{ALL}}^2 + \max(\chi_{\text{BLZ}}^2, \chi_{\text{BLL}}^2 + \chi_{\text{FSRQ}}^2). \quad (14)$$

The upper bound from ALL is implemented as:

$$\chi_{\text{ALL}}^2 = \sum_i \left[\max \left(\frac{\langle \frac{dN}{dS} \rangle_{\text{BLZ},i} - \left(\frac{dN}{dS} \right)_{\text{ALL},i}}{\sigma_{\text{ALL},i}}, 0 \right) \right]^2. \quad (15)$$

Here, the dN/dS in angle brackets denotes the model prediction from Equation (12), and the dN/dS in round brackets is the source count distribution extracted from the 4FGL catalog. The model includes the sum of the BLLs and FSRQs, namely $\langle dN/dS \rangle_{\text{BLZ},i} = \langle dN/dS \rangle_{\text{BLL},i} + \langle dN/dS \rangle_{\text{FSRQ},i}$. For this contribution, we integrate over all redshifts and all values of the photon spectral index. The remaining index i denotes the flux bin, as summarized in Table 1. If the flux of the bin is below the detection threshold S_{thr} , the bin is excluded from the sum.

For the lower bounds, which relate to identified or associated blazars, we would also like to consider the redshift information, which is not directly provided in the 4FGL catalog. So we extract the information from the 4LAC catalog (Ajello et al. 2020), which contains spectroscopic redshift measurements. However, the redshift information in the 4LAC catalog is incomplete, i.e., not all sources have a redshift measurement.

Since we only consider the identified or associated blazars as a lower bound, this does not represent a problem, but it might not be the most constraining option. Hence, we again consider two cases. In the first case, we include redshift information and compare our model in bins of a two-dimensional grid in redshift and flux through

$$\chi_{\text{BLZ},S_z}^2 = \sum_{ij} \left[\min \left(\frac{\langle \frac{dN}{dS} \rangle_{\text{BLZ},ij} - \left(\frac{dN}{dS} \right)_{\text{BLZ},ij}}{\sigma_{\text{BLZ},ij}}, 0 \right) \right]^2. \quad (16)$$

In the second case, we disregard the redshift information by integrating over the redshift. We define

$$\chi_{\text{BLZ},S}^2 = \sum_i \left[\min \left(\frac{\langle \frac{dN}{dS} \rangle_{\text{BLZ},i} - \left(\frac{dN}{dS} \right)_{\text{BLZ},i}}{\sigma_{\text{BLZ},i}}, 0 \right) \right]^2. \quad (17)$$

Depending on the model parameter point, either Equation (16) or Equation (17) provides the stronger constraint. Similar to the discussion above, we cannot use the sum of both χ^2 s, due to double counting, so again we choose the most constraining one:

$$\chi_{\text{BLZ}}^2 = \max(\chi_{\text{BLZ},S_z}^2, \chi_{\text{BLZ},S}^2). \quad (18)$$

As described in Equation (14), we select the lower bounds by comparing χ_{BLZ}^2 with the ones from the analysis of the individual BLL and FSRQ source classes. In this latter case, we can use the full information from the catalogs and compare the models with the data from a three-dimensional grid of flux, redshift, and photon spectral index. Again, since the redshift information is incomplete, we define the χ^2 as the maximum of the two cases:

$$\chi_M^2 = \max(\chi_{M,S_z\Gamma}^2, \chi_{M,S\Gamma}^2), \quad (19)$$

where M stands for either BLL or FSRQ. The individual χ^2 s in the two cases are defined by

$$\chi_{M,S_z\Gamma}^2 = \sum_{i,j,k} \left[\min \left(\frac{\langle \frac{dN}{dS} \rangle_{M,ijk} - \left(\frac{dN}{dS} \right)_{M,ijk}}{\sigma_{M,ijk}}, 0 \right) \right]^2, \quad (20)$$

when redshift information is included, and by

$$\chi_{M,S\Gamma}^2 = \sum_{i,k} \left[\min \left(\frac{\langle \frac{dN}{dS} \rangle_{M,ik} - \left(\frac{dN}{dS} \right)_{M,ik}}{\sigma_{M,ik}}, 0 \right) \right]^2 \quad (21)$$

in the case with the flux and spectral index bins only.

To avoid a bias from the Galactic plane, we exclude small latitudes with $|b| < 30^\circ$ from our analysis.

2.3.2. Fit to the C_p Data

The fit of the APS is performed on the autocorrelation ($i = j$) and cross-correlation ($i \neq j$) measurements, where i and j denote the energy bins. The $\chi_{C_p}^2$ is defined as

$$\chi_{C_p}^2 = \sum_{i \leq j} \frac{[(C_p^{ij})_{\text{meas}} - (C_p^{ij})_{\text{th}}]^2}{\sigma_{C_p^{ij}}^2}. \quad (22)$$

The subscript *meas* refers the measured C_P obtained in Ackermann et al. (2018), while the subscript *th* denotes the theoretical estimation of C_P calculated as in Equation (9). Finally, $\sigma_{C_P}^2$ are the uncertainties of the measured C_P , again taken from Ackermann et al. (2018).

2.4. Analysis Strategy

As anticipated above, we perform two fits in this work. The first one utilizes only the 4FGL catalog, while the second one additionally uses the C_P measurement. The basic idea is as follows. From the first fit, we obtain constraints on the GLF and SED models of the two blazar populations in the flux regime of resolved point sources. From there, we can extrapolate to the unresolved flux regime and calculate the C_P . As will become clear in Section 2.5, this extrapolation agrees well with the actual C_P measurement. As such, we can go one step further and also perform the second fit, which combines the resolved point sources (4FGL) with the C_P . This combined fit provides GLF and SED models that are consistent with the gamma-ray observations below the flux threshold of the 4FGL catalog. When we derive the DM constraints in Section 3, the combined fit serves as the baseline.

The large parameter space investigated in this work is sampled using MULTINEST (Feroz et al. 2009). We use a configuration with 800 live points, an enlargement factor of $\text{efr}=0.7$, and a stopping parameter of $\text{tol}=0.1$. In the following, we present the results in the Bayesian statistical framework.

2.5. Results for the GLF and SED of BLLs and FSRQs

As a result of our fits, we obtain the GLFs and SEDs of the FSRQs and BLLs. The 4FGL categorization of the blazars into the two classes is incomplete, which leaves some degeneracy. We allow the fit to attribute the uncharacterized blazars either to the BLLs or FSRQs. This is only possible because we fit both source classes at the same time. We note that this treatment leads to correlations of BLL parameters with FSRQ parameters and vice versa. These correlations are important for correctly assessing the uncertainty of the full blazar model, as, for example, in Section 3, where blazars constitute the background for our DM search.

The results are summarized in Table 2, where we state the mean values and the 1σ uncertainty derived from the marginalized posterior for each parameter. Results are provided for two setups. In the first setup, we only fit the resolved point sources of the 4FGL catalog, while in the second setup, we fit both the resolved sources and the APS data. The obtained parameter values of the two setups are compatible within their uncertainties. The GLF parameters of the FSRQ and BLL models are well compatible with the parameter values of Ajello et al. (2012) and Ajello et al. (2014), respectively. This means that the GLF of the sources belonging to the fainter regime probed in this work closely follow the one of the brighter end. We note that we use a slightly different definition of the LDDE than Ajello et al. (2012), which leads to slightly different parameter values for p_1^* , p_2^* , and z_c^* .

Figure 2 shows the best fits and uncertainties of the dN/dS from the combined fit to 4FGL+ C_P in comparison to the dN/dS extracted from the 4FGL catalog. The four different panels correspond to the different contributions to χ_{4FGL}^2 . In more detail, the data points in the upper left panel show the dN/dS of

Table 2
The Fit Results of the GLFs

	4FGL fit		4FGL+ C_P fit	
	FSRQ	BLL	FSRQ	BLL
$\log_{10}(A [\text{Mpc}^{-3}])$	$-9.35_{-0.37}^{+0.62}$	$-9.80_{-1.11}^{+0.40}$	$-9.65_{-0.47}^{+0.61}$	$-9.01_{-1.11}^{+1.21}$
$\log_{10}(L^* [\text{erg/s}])$	$48.36_{-0.66}^{+0.31}$	$47.85_{-0.52}^{+0.79}$	$48.53_{-0.60}^{+0.42}$	$47.26_{-1.09}^{+0.75}$
γ_1	$0.57_{-0.09}^{+0.15}$	$1.03_{-0.07}^{+0.12}$	$0.72_{-0.09}^{+0.13}$	$0.92_{-0.07}^{+0.18}$
γ_2	$1.93_{-0.43}^{+0.14}$	$1.95_{-0.45}^{+0.16}$	$1.97_{-0.42}^{+0.21}$	$1.88_{-0.38}^{+0.12}$
z_c^*	$0.92_{-0.27}^{+0.20}$	$1.05_{-0.53}^{+0.16}$	$0.87_{-0.24}^{+0.14}$	$1.06_{-0.56}^{+0.16}$
p_1^*	$5.86_{-5.02}^{+2.15}$	$7.48_{-4.51}^{+3.97}$	$8.37_{-3.35}^{+3.78}$	$4.01_{-3.54}^{+0.77}$
p_2^*	$-0.88_{-0.14}^{+0.77}$	$-1.97_{-0.43}^{+1.83}$	$-0.77_{-0.11}^{+0.67}$	$-0.93_{-0.19}^{+0.83}$
α	$0.20_{-0.16}^{+0.07}$	$0.28_{-0.13}^{+0.14}$	$0.11_{-0.11}^{+0.02}$	$0.31_{-0.07}^{+0.17}$
μ^*	$2.50_{-0.04}^{+0.03}$	$2.03_{-0.04}^{+0.04}$	$2.49_{-0.04}^{+0.03}$	$2.05_{-0.04}^{+0.03}$
σ	$0.19_{-0.04}^{+0.02}$	$0.22_{-0.05}^{+0.03}$	$0.20_{-0.04}^{+0.02}$	$0.19_{-0.03}^{+0.02}$
β		$0.06_{-0.05}^{+0.02}$		$0.03_{-0.03}^{+0.01}$
k_{C_P}			$1.09_{-0.12}^{+0.16}$	
χ_{ALL}^2		1.7		2.9
χ_{BLZ}^2		3.0		2.7
χ_{BLL}^2		11.4		12.7
χ_{FSRQ}^2		7.4		8.0
χ_{4FGL}^2		20.5		26.3
$\chi_{C_P}^2$				81.0
χ^2		20.5		107.3

all sources from the 4FGL catalog (at $|b| > 30^\circ$). The sum of our models for the BLLs and FSRQs is in agreement with those data. Because of the statistical technique that we adopted (see above), it is expected to stay at the level or below those data points. The open white data point is below the flux threshold, so it is excluded from the analysis. The upper right panel shows the data points of the dN/dS for all identified or associated blazars. The different colors show the dN/dS in different redshift bins, while the black points are summed over all redshifts. Our model for the dN/dS of the BLLs plus FSRQs lies, as expected, at the level or above the data points. In both upper panels, the source count distribution is integrated over all photon spectral indices, from 1.0 to 3.5. Furthermore, the upper panels only show the constraints from the 4FGL catalog on the sum of the BLL and FSRQ models. The two lower panels, instead, look at the individual models for FSRQs and BLLs. Furthermore, they focus on the dN/dS for specific bins of the photon spectral index, corresponding to the peak of the distribution for each class. The lower left panel compares the dN/dS BLLs in the Γ bin from 1.9 to 2.1. Again, the different colors correspond to different redshift bins, and the black points contain the sum over all redshifts. Finally, the lower right panel is the same as the left panel, but for FSRQs and a Γ bin from 2.4 to 2.6. All in all, we see that our model matches the constraints from the 4FGL catalog very well. We show these plots only for the 4FGL+ C_P fit, but we note that they look very similar for the 4FGL-only fit.

Figure 3 compares the C_P measurement with the best-fit model and uncertainty from the 4FGL+ C_P setup. The left panel shows the C_P autocorrelation, while the right panel shows an example of cross-correlation, between the (8.3, 14.5) GeV energy bin and all other energy bins. The sum of the BLL and FSRQ models provides a good fit to the data. This was also the case in the analysis of unresolved sources after 2 yr of Fermi-LAT data (Di Mauro et al. 2014). In the meantime, however,

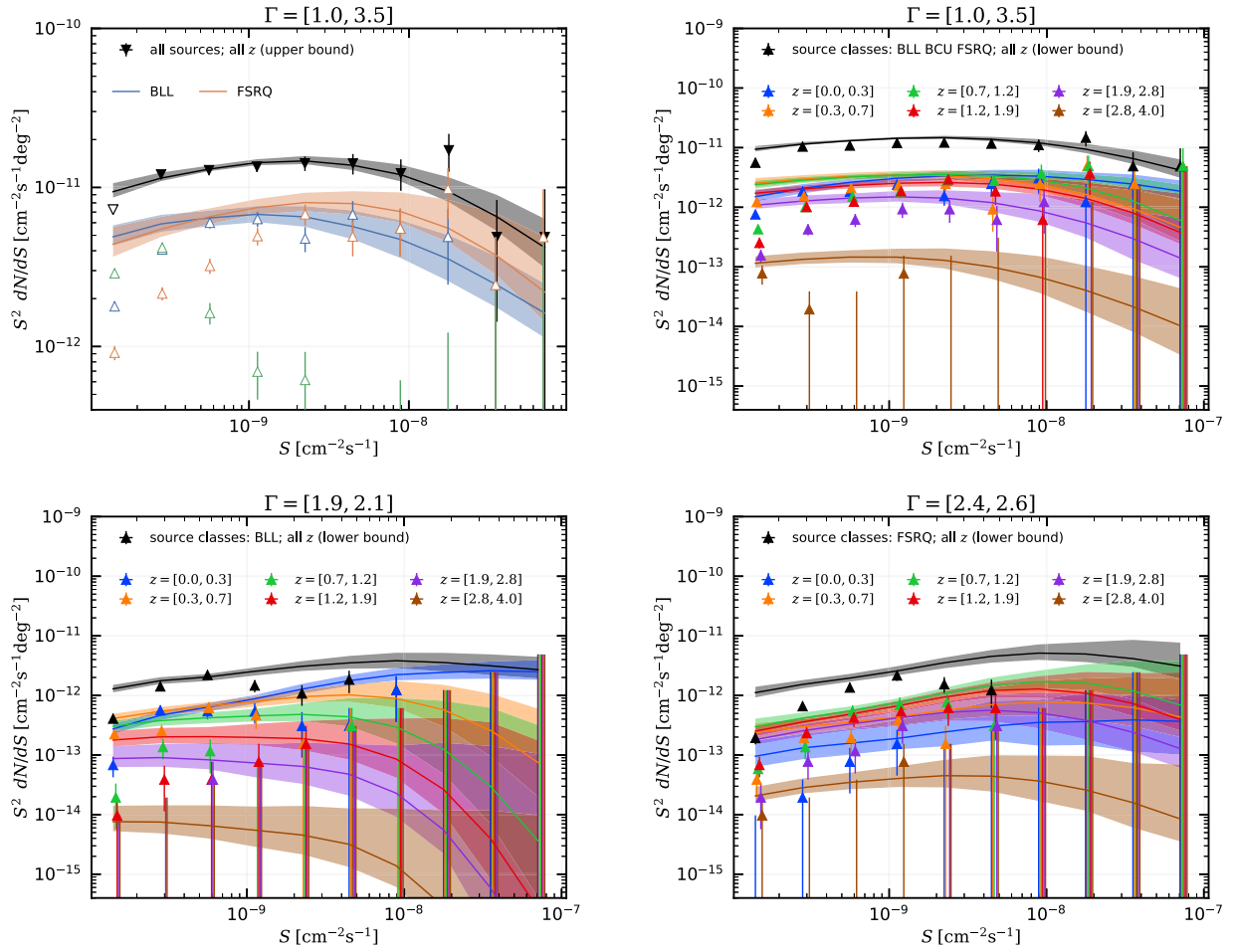


Figure 2. Source count distributions of the 4FGL sources in bins of flux (S), photon spectral index (Γ), and redshift (z). The GLF is fitted to 4FGL+ C_P . The band shows the 1σ Bayesian uncertainty. The black open (filled white) data point in the upper left panel is below the flux threshold and thus not included in the fit (see the text for further details). In our statistical analysis, the data in the upper left panel are taken as the upper bounds, while for all the other panels they are the lower bounds. The colored open data points show the identified BLLs (blue), FSRQs (orange), and BCUs (green). Those points are not included in the fit and are only shown for comparison.

many more point sources were resolved and the C_P measurement decreased by a factor of about 10, making the latest data much more sensitive to faint populations. Still, we find that blazars explain the entire latest C_P measurement. The feature at 200 GeV in our model (and also, less visible, in the data) is related to a change in the analysis adopted for the measurement from Ackermann et al. (2018): for energies below 200 GeV, bright point sources are masked from the 4FGL catalog, but in the last two bins at high energies, bright point sources are masked using the 3FHL catalog. This leads to a change in the actual S_{thr} , which explains the feature. The feature does not appear in the right panel because for the cross-correlation the masks of the two energy bins involved in the measurement were joined (so when an energy bin below 200 GeV is present, the mask is mostly provided by the point sources of the 4FGL catalog). Note also from Table 2 that the nuisance parameter k_{C_P} , introduced to allow for a possible rescaling of the flux threshold sensitivity from the reference model, is within uncertainties compatible with the default value of 1.

It is also interesting to look at the 4FGL-only setup, and to use the extrapolation of the GLF and SED model to predict the C_P . As shown in Figure 4, our prediction agrees very well with the measurement. We note that the C_P is dominated by FSRQs at low energies, below ~ 2 GeV, while BLLs dominate at

higher energies. The domination of BLLs at high energies is expected, since they have a harder SED than FSRQs. The fact that there is a transition from FSRQs to BLLs in the C_P at low energies introduces a softening in the spectral index at low energies. This softening has previously been interpreted as a possible hint of a new source population (Ando et al. 2017). The new C_P data (Ackermann et al. 2018), and the detailed treatment presented here, allow us to interpret it in terms of FSRQs.

Figure 4 already hints that both BLLs and FSRQs are required to describe the C_P data. We better quantify this statement in the following. Using the results of the 4FGL-only fit, we calculate the posterior distribution of the $\chi^2_{C_P}$, assuming (i) the sum of the FSRQs and BLLs, labeled all, and (ii) only the BLLs. An FSRQ-only hypothesis is excluded, since it cannot explain the high-energy C_P data. In order to consider the systematic uncertainty on the exact flux threshold, we profile over the normalization of the C_P . The results in Figure 5 show that the sum of the FSRQs and BLLs is preferred. Using the full posterior of the 4FGL-only fit, and defining $\mathcal{L}_{C_P} = \exp(-\chi^2_{C_P}/2)$, we calculate the Bayes factors of hypotheses (i) and (ii), obtaining 4.0×10^3 . More details about the calculation of the Bayes factors are given in Appendix B. In this sense, the two physical populations (BLLs and FSRQs) are

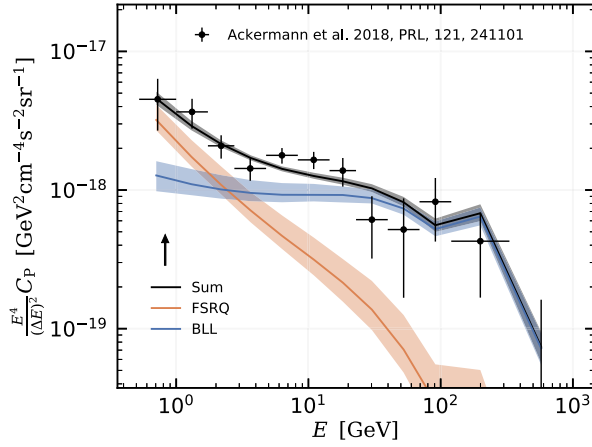


Figure 3. Angular correlation of the 4FGL+ C_p fit. The shaded bands mark the 1σ Bayesian uncertainty.

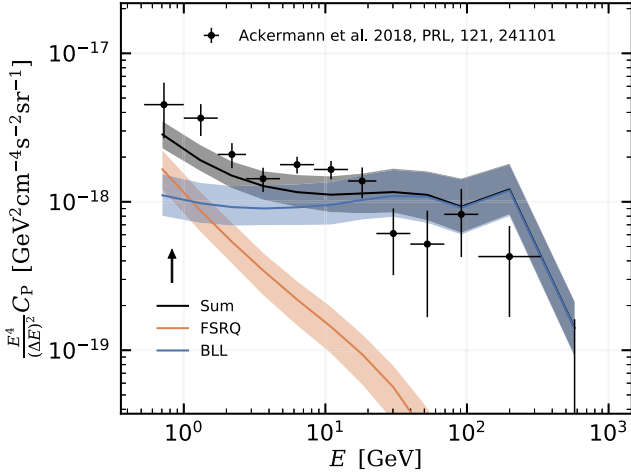
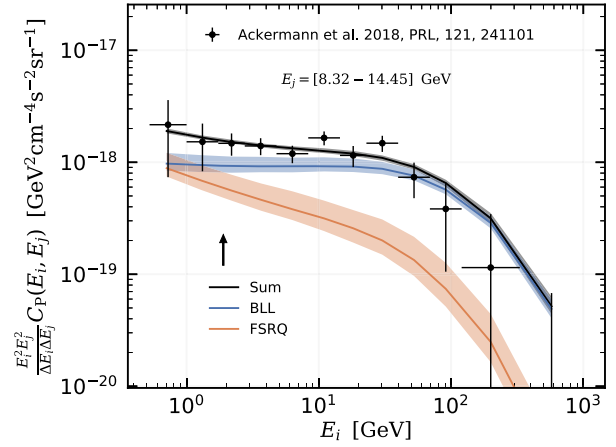


Figure 4. The GLF is fitted to 4FGL sources and then extrapolated to the C_p . The band shows the 1σ Bayesian uncertainty.

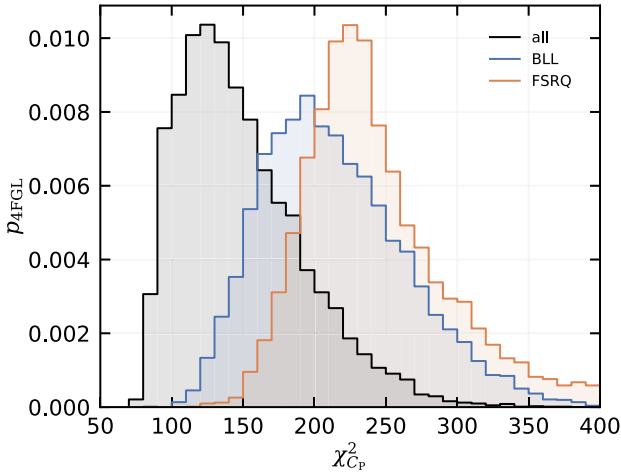


Figure 5. Posterior distribution of the 4FGL-only fit for the $\chi^2_{C_p}$. We show the distributions for three cases: considering the sum of the BLLs and FSRQs (all), only the BLLs (BLL), and only the FSRQs (FSRQ).

clearly preferred over a single population of only BLLs or only FSRQs. We note, however, that the preference for these two populations is based on the catalog prior. As discussed in Appendix A, the C_p data are not sufficient to distinguish between a scenario with one or two populations. Without the

catalog prior, a hypothetical and more general GLF and SED can provide a good fit to the C_p data.

Finally, Figure 6 shows a triangle plot with posterior distributions for the parameters of the GLF and SED for the BLL and FSRQ models. The posteriors correspond to the 4FGL+ C_p setup. The diagonal contains the marginalized one-dimensional posteriors for each individual parameter, while the panels in the lower half show the 1σ and 2σ contours for each combination of two parameters. Since the BLL and FSRQ models have the same functional form, we can combine them into the same triangle, using different colors. We observe that the SED parameters μ^* and σ are well constrained for both populations. The average photon spectral index of the BLLs is $\mu^* \sim 2.0$, with a width of $\sigma \sim 0.2$. As expected, the FSRQs follow a softer energy spectrum, with an average index of $\mu^* \sim 2.5$ and a similar width. Also, the shape of the GLF at small L is reasonably constrained. The index γ_1 lies between 0.4 and 1.0 for the FSRQs and between 0.5 and 1.2 for the BLLs, while the behavior at large L (see γ_2) is less constrained. We note the degeneracy between A and L^* . This is because, in both cases, at first order, their main impact on the fit is to change the normalization of the GLF. The redshift dependence is only weakly constrained due to degeneracies with other parameters.

We provide the covariance matrix of our fits in the ancillary files (arXiv version). This covers, to a first approximation, the degeneracies and correlations of the fit parameters. As a final comment, let us note that, clearly, the uncertainties on the parameters of the BLLs and FSRQs show some level of mutual correlation in the fit. It is only for the sake of clarity that we do not show the entire triangle plot in Figure 6.

2.6. Blazar Contribution to the UGRB

We see that the measured gamma-ray angular correlations require the presence of FSRQs and BLLs. Populations with a GLF peaked at lower luminosities (like mAGNs and SFGs) cannot account for the C_p data. Thus, FSRQs and BLLs provide an inescapable contribution to the UGRB intensity. In Figure 7, we compare the UGRB measurement of Fermi-LAT from Ackermann et al. (2015) with the prediction from our models. The measurement accounted for the contribution of point sources from the 2FGL catalog (Nolan et al. 2012). To be consistent, we apply a flux threshold corresponding to the 2FGL catalog, taken from Ackermann et al. (2015), for the

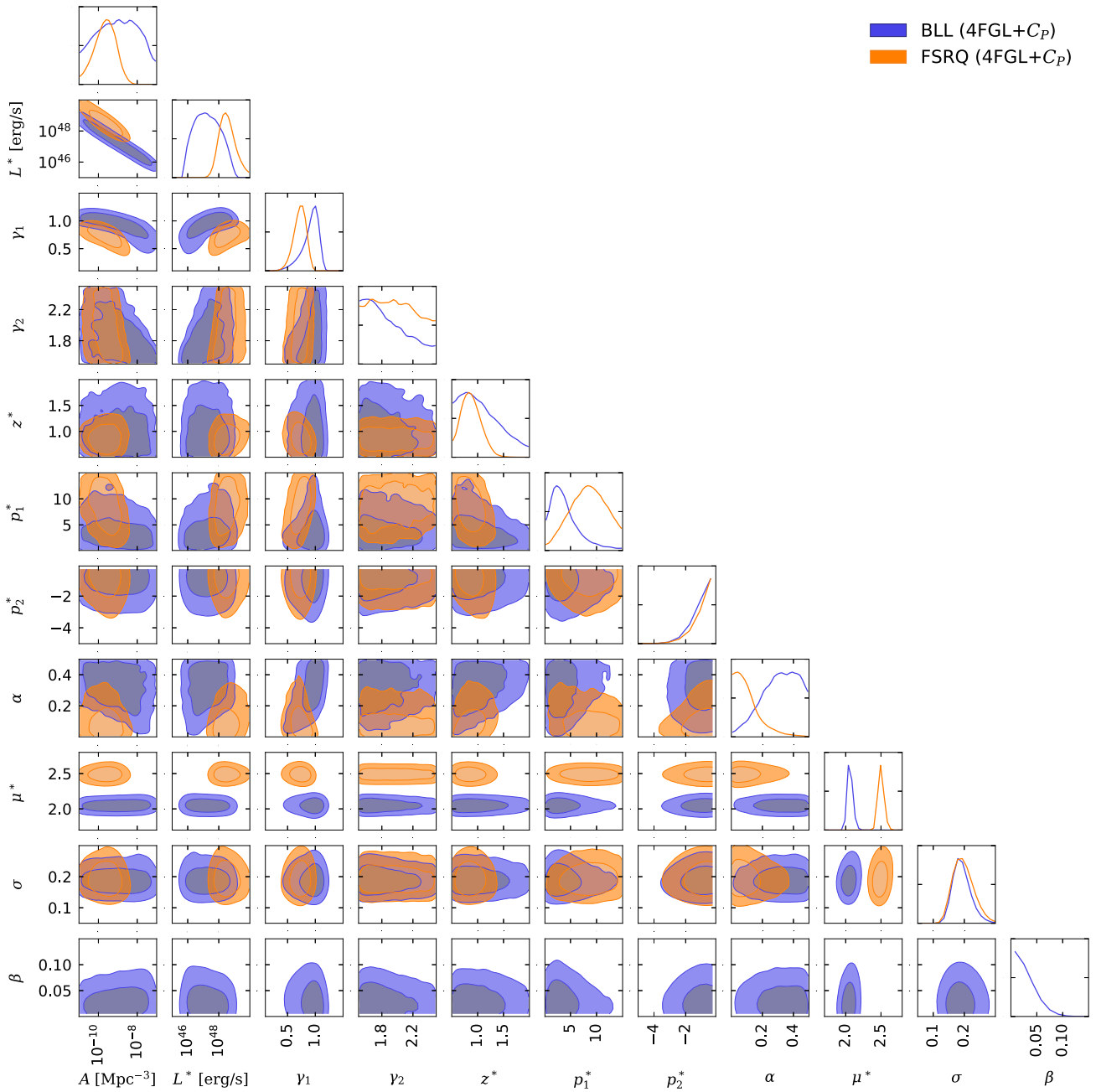


Figure 6. Triangle showing the parameter constraints of the GLF of the FSRQs (amber) and BLLs (blue). Both constraints are derived from the fit to the 4FGL+ C_p data. The panels on the diagonal show the marginalized posterior distributions of each single parameter, while the panels in the lower half show the 1σ and 2σ uncertainty contours derived from the two-dimensional marginalized posterior for each combination of two parameters.

predictions in Figure 7. We conclude that blazars provide a significant contribution to the UGRB, accounting for about 30% between 10 and 100 GeV. At energies below 1 GeV, the contribution decreases to about 20%.

3. Bounds on WIMP DM

The UGRB observed by Fermi-LAT could conceal a signal from DM particles. We focus our analysis on annihilating DM. Since annihilation occurs universally in all DM structures, we need to consider the gamma-ray emission from both the halo of our galaxy and from extragalactic structures. We therefore have two DM contributions to the anisotropy APS, one for the Galactic halo and one from the extragalactic DM distribution (the two contributions are not expected to cross-correlate).

Moreover, extragalactic structures host the same astrophysical sources (BLLs and FSRQs) that we have discussed in previous sections. This induces a cross-correlation term in the APS between extragalactic DM and source emissions. All these terms are properly modeled and taken into account in our analysis, as outlined below. In the following, we will discuss the contribution of DM only to the anisotropy signal C_p , since the contribution of DM halos to the source count distribution is significantly suppressed as compared to that arising from astrophysical sources in the resolved flux regime. A DM contribution to the dN/dS could, in principle, emerge on top of astrophysical sources only at very low fluxes.

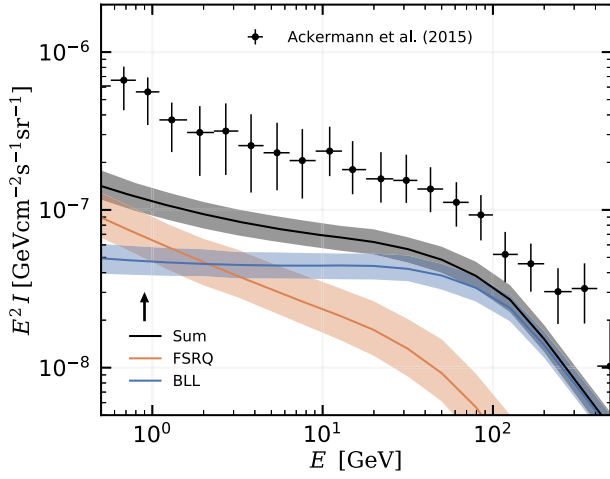


Figure 7. Contribution of BLLs and FSRQs to the UGRB intensity. The flux threshold corresponds to the 2FGL catalog, both for the data points and the model prediction. The band shows the 1σ Bayesian uncertainty.

3.1. Extragalactic DM Modeling

The APS of the cross-correlation between a source field X in the energy bin i and a source field Y in the energy bin j reads (Fornengo & Regis 2014)

$$C_\ell^{X,Y} = \int \frac{d\chi}{\chi^2} W_i^X(\chi) W_j^Y(\chi) P^{XY}(k = \frac{\ell}{\chi}, \chi), \quad (23)$$

where $W^X(\chi)$ is the window function of the field X , $P^{XY}(k, \chi)$ is the three-dimensional cross-power spectrum of the fluctuations of the two fields, and χ denotes the comoving distance, related to redshift by $d\chi = (c dz)/H(z)$.

The window function for annihilating DM is given by (Ando & Komatsu 2006; Fornengo & Regis 2014)

$$W_{\text{DM}}(z, E) = \frac{(\Omega_{\text{DM}} \rho_c)^2 \langle \sigma_{\text{ann}} v \rangle}{4\pi 2m_{\text{DM}}^2} (1+z)^3 \Delta^2(z) \times \frac{dN_{\text{ann}}}{dE} [E(1+z)] e^{-\tau[z, E(1+z)]}, \quad (24)$$

where Ω_{DM} and ρ_c are the present-day cosmological abundance of DM and the critical density of the universe, respectively, m_{DM} is the mass of the DM particle, $\Delta^2(z)$ is the clumping factor, and $\langle \sigma_{\text{ann}} v \rangle$ denotes the velocity-averaged annihilation cross section of DM particles, assumed here to be the same in all DM halos. dN_{ann}/dE indicates the number of photons produced per annihilation as a function of energy, and sets the gamma-ray energy spectrum, and $\tau(E, z)$ denotes the optical depth of the gamma-ray photons, which we model as in Finke et al. (2010).

To determine the DM autocorrelation, we compute the three-dimensional power spectrum with the so-called halo model approach (see, e.g., the review in Cooray & Sheth 2002). For

$X = Y = \text{DM}$, we have

$$P_{\text{DM,DM}}^{\text{1h}}(k, z) = \int_{M_{\text{min}}}^{M_{\text{max}}} dM \frac{dn_{\text{h}}}{dM} \left(\frac{\hat{u}_{\kappa}(k|M, z)}{\Delta^2(z)} \right)^2$$

$$P_{\text{DM,DM}}^{\text{2h}}(k, z) = \left[\int_{M_{\text{min}}}^{M_{\text{max}}} dM \frac{dn_{\text{h}}}{dM} b_{\text{h}} \frac{\hat{u}_{\kappa}(k|M, z)}{\Delta^2(z)} \right]^2 \times P^{\text{lin}}(k, z), \quad (25)$$

where dn_{h}/dM is the halo mass function, $P^{\text{lin}}(k, z)$ is the linear matter power spectrum, $b_{\text{h}}(M)$ is the linear bias, and $\hat{u}_{\text{ann}}(k|M, z)$ denotes the Fourier transform of the density profile of the DM halos (see, e.g., see the Appendix of Cuoco et al. 2015). We assume the Navarro–Frenk–White (NFW) DM density profile (Navarro et al. 1996). All the ingredients in Equations (24) and (25) are modeled as in Ammazzalorso et al. (2020). The minimal and maximal halo masses are set at $M_{\text{min}} = 10^{-6} M_{\odot}$ and $M_{\text{max}} = 10^{18} M_{\odot}$, respectively.

To characterize the halo profile and the subhalo contribution, we need to specify their mass concentration. The description of the concentration parameter $c(M, z)$ at small masses and for subhalos is still an open issue, and provides our largest source of uncertainty. In the following, we consider two models that we name “LOW,” where we take the description of $c(M, z)$ from Correa et al. (2015), and “HIGH,” where we follow Neto et al. (2007). They differ as to what concerns the extrapolation of the concentration at low masses, leading to a difference of about one order of magnitude in the final bounds on the annihilation cross section, as shown in Section 3.4.

Clearly, the distribution of the extragalactic DM halos (and, in turn, of the annihilation signal) has some level of correlation with the blazar distribution, therefore inducing a cross-correlation signal between DM and the blazars. The blazar window function can be phrased as $W_{\text{BLA}}(z, E) = \chi(z)^2 \langle f_{\text{S}} \rangle$, with the mean flux defined as

$$\langle f_{\text{S}} \rangle = \int_1^{3.5} d\Gamma \int_{L_{\text{min}}}^{L_{\text{max}}} dL_{\gamma} \Phi_{\text{S}}(L_{\gamma}, z, \Gamma) \times S(L_{\gamma}, z, \Gamma) (1 - \Omega). \quad (26)$$

The three-dimensional power spectrum of the cross-correlation between annihilating DM and the blazars is given by

$$P_{\text{BLA,DM}}^{\text{1h}}(k, z) = \int_1^{3.5} d\Gamma \int_{L_{\text{min}}}^{L_{\text{max}}} dL_{\gamma} \frac{\Phi(L_{\gamma}, z, \Gamma)}{\langle f_{\text{S}} \rangle} \times S(L_{\gamma}, z, \Gamma) (1 - \Omega) \frac{\hat{u}_{\kappa}(k|M(L_{\gamma}, z))}{\Delta^2(z)}, \quad (27)$$

$$P_{\text{BLA,DM}}^{\text{2h}}(k, z) = \int_{M_{\text{min}}}^{M_{\text{max}}} dM \frac{dn_{\text{h}}}{dM} b_{\text{h}} \frac{\hat{u}_{\kappa}(k|M, z)}{\Delta^2(z)} \times \int_1^{3.5} d\Gamma \int_{L_{\text{min}}}^{L_{\text{max}}} dL_{\gamma} b_{\text{S}} \frac{\Phi(L_{\gamma}, z, \Gamma)}{\langle f_{\text{S}} \rangle} S(L_{\gamma}, z, \Gamma) (1 - \Omega) \times P^{\text{lin}}(k, z), \quad (28)$$

where b_{S} is the bias of the blazars with respect to the matter density, for which we adopt $b_{\text{S}}(L_{\gamma}, z) = b_{\text{h}}[M(L_{\gamma}, z)]$. The relation $M(L_{\gamma}, z)$ between the mass of the host halo and the luminosity of the hosted blazar is taken from Camera et al. (2015).

3.2. Galactic DM Modeling

For the modeling of the signal expected from the Galactic subhalos, we follow the treatment of Ando (2009). In general, the prediction of the APS for the Galactic component is the sum of two contributions, one arising from the main halo and the other originating from substructures. The main (smooth) halo contribution is subdominant for multipoles above a few: since we are dealing with multipoles larger than 50, it is here neglected. For the substructure contribution, we consider an unbiased subhalo distribution, corresponding to fiducial model A1 of Ando (2009), with a boost factor for subhalos set to unity.

The subhalo number density as a function of the distance f from the center of the galaxy reads

$$n_{\text{sh}}(r) = f \frac{M_{\text{vir,MW}}}{2\pi r_{-2}^3 M_{\text{min}}} \gamma\left(\frac{3}{\alpha_E}, \frac{2c_{-2}}{\alpha_E}\right)^{-1} \left(\frac{2}{\alpha_E}\right)^{3/\alpha_E-1} \times \exp\left[-\frac{2}{\alpha_E} \left(\frac{r}{r_{-2}}\right)^{\alpha_E}\right], \quad (29)$$

where $M_{\text{vir,MW}}$ is the Milky Way virial mass, $\alpha_E = 0.68$, γ is the lower incomplete gamma function, $r_{-2} = 0.81 r_{200,\text{MW}}$, $c_{-2} = r_{\text{vir}}/r_{-2}$, and the fraction f of DM enclosed in subhalos is fixed to 0.2. The minimal subhalo mass is set at $M_{\text{min}} = 10^{-6} M_{\odot}$. We do not include a truncation for the subhalo distribution at large radii. The angle average number density referred to our position in the galaxy is

$$\bar{n}_{\text{sh}} = \frac{1}{2} \int_{-1}^1 d\cos(\psi) n_{\text{sh}}(r(\cos\psi)), \quad (30)$$

where $r(\cos(\psi)) = \sqrt{r_0^2 + s^2 - 2r_{\oplus}s\cos(\psi)}$, $r_{\oplus} = 8.5$ kpc is our distance from the center of the galaxy, s represents the distance along the line of sight, and ψ is the angle between the direction \hat{n} of observation and the direction to the Galactic center.

Numerical simulations suggest that the mass distribution of subhalos follows a power-law behavior with the mass M of the subhalo, and can be written as

$$\frac{d\bar{n}_{\text{sh}}}{dM} = \bar{n}_{\text{sh}}(r) \frac{\alpha_0 - 1}{M_{\text{min}}} \left(\frac{M}{M_{\text{min}}}\right)^{-\alpha_0}, \quad (31)$$

where $\alpha_0 = 1.9$.

The subhalo luminosity L for a subhalo with mass M depends on the particle properties of DM, $\langle\sigma_{\text{ann}}v\rangle$ and m_{DM} , as well as on the energy spectrum dN_{ann}/dE associated with the channel under study. It reads

$$L = \frac{\langle\sigma_{\text{ann}}v\rangle M^2}{24\pi m_{\chi}^2 r_s^3} \int dE \frac{dN_{\text{ann}}}{dE}. \quad (32)$$

With the above ingredients, the APS for the Galactic subhalo contribution can then be expressed as

$$C_{\ell}^{ij} = \frac{1}{16\pi^2 f_{\text{sky}}} \int_{M_{\text{min}}}^{M_{\text{max}}} dM \int_{s_{\text{min}}}^{s_{\text{max}}} ds \frac{L^i(M) L^j(M)}{s^2} \times \frac{d\bar{n}_{\text{sh}}}{dM} \tilde{u}_{\text{sh}}^2\left(\frac{\ell}{s}, M\right), \quad (33)$$

where i and j refer to energy bins. The integral along the line of sight is performed up to $s_{\text{max}} = r_{\text{vir,MW}} = 258$ kpc, and starts at

$s_{\text{min}} = \sqrt{L/(4\pi S_{\text{thr}})}$. In this specific case, we use a simplified approach: instead of the full, i.e., Γ -dependent, flux threshold, we use a fixed threshold averaged over Γ . More specifically, the thresholds (corresponding to the flux from 1 to 100 GeV) are set to $S_{\text{thr}} = 10^{-10} \text{cm}^{-2} \text{s}^{-1}$ for the first 10 energy bins (the 4GFL threshold) and $2 \times 10^{-10} \text{cm}^{-2} \text{s}^{-1}$ for the two highest energy bins (the 3FHL threshold). The value of s_{min} is thus chosen such that only unresolved Galactic subhalos are considered in the determination of the APS. We adopted an NFW profile for the internal density distribution of the subhalos, and \tilde{u}_{sh} denotes its Fourier transform. The maximal halo mass for the subhalos in our galaxy $M_{\text{max}} = 10^{10} M_{\odot}$.

In summary, the APS involving DM is given by the sum of four terms—three extragalactic terms (the autocorrelation from the extragalactic DM halos and the cross-correlations with the BLLs and FSRQs) and the Galactic term, which is not expected to cross-correlate with extragalactic source populations. Since the DM contributions are not flat in multipole, but ℓ -dependent, they are averaged in the multipole range considered for the determination of the C_{P} measurement in Ackermann et al. (2018).

3.3. Statistical Framework

We derive bounds on the DM annihilation cross section as a function of the DM mass by marginalizing over the uncertainties in the astrophysical background model. This means that we are not using the approximation of a fixed background model obtained from the best fit of the blazar-only case, on top of which the DM contribution is added.

The naive approach to considering the full uncertainty would be to perform an extended parameter scan, which would include the blazar parameters and the DM parameters at the same time. However, this is computationally very expensive. We instead use a method called ‘‘importance sampling’’ in order to recycle the information from background-only fits, which significantly speeds up the calculation. The same approach has recently been used in a different context (Kahlhoefer et al. 2021).

One by-product of the MULTINEST scan is a set of parameter vectors that follows the multidimensional posterior distribution. This set is provided in the so-called equal-weights sample. We will apply importance sampling to obtain the posterior distribution of the full parameter space (blazars and DM) by using the equal-weights set of the fit to blazars only.

First, we note that we can approximate the integral of the product of the background, i.e., the blazar, posterior, and an arbitrary function f over the blazar parameters, θ_{blz} , by a sum over the parameter points in the set of the equal-weights sample:

$$\int d\theta_{\text{blz}} \frac{\mathcal{L}_0(\theta_{\text{blz}}) p_0(\theta_{\text{blz}})}{Z_0} f(\theta_{\text{blz}}) \approx \frac{1}{N} \sum_{i=1}^N f(\theta_{\text{blz},i}), \quad (34)$$

where \mathcal{L}_0 is the likelihood, Z_0 is the evidence, and p_0 is the prior. The subscript 0 indicates quantities that refer to the fit without DM. We note that the factor $\mathcal{L}_0(\theta_{\text{blz}}) p_0(\theta_{\text{blz}})/Z_0$ is by definition the posterior distribution. Furthermore, we know that the integral over the prior $p_0(\theta_{\text{blz}})$ is normalized to 1. If we set

$f(\theta_{\text{blz}}) = Z_0/\mathcal{L}_0(\theta_{\text{blz}})$, we see that the evidence is given by

$$Z_0 = \frac{N}{\sum_{i=1}^N 1/\mathcal{L}_0(\theta_{\text{blz},i})}. \quad (35)$$

We can obtain the marginalized likelihood by integrating over the background parameters:

$$\tilde{\mathcal{L}}(\theta_{\text{DM}}) = \int d\theta_{\text{blz}} \mathcal{L}(\theta_{\text{blz}}, \theta_{\text{DM}}) p(\theta_{\text{blz}}). \quad (36)$$

Here, $\theta_{\text{DM}} = \{m_{\text{DM}}, \langle\sigma_{\text{ann}}v\rangle\}$ denotes the DM parameters, $\mathcal{L}(\theta_{\text{blz}}, \theta_{\text{DM}})$ is the likelihood of the full parameter space, and $p(\theta_{\text{blz}})$ is the prior of the blazar parameters. Using Equation (34), and assuming the same prior ($p(\theta_{\text{blz}}) = p_0(\theta_{\text{blz}})$), we see that the integral of Equation (36) is approximately given by the sums

$$\tilde{\mathcal{L}}(\theta_{\text{DM}}) \approx \frac{\sum_{i=1}^N \frac{\mathcal{L}(\theta_{\text{blz},i}, \theta_{\text{DM}})}{\mathcal{L}_0(\theta_{\text{blz},i})}}{\sum_{i=1}^N \frac{1}{\mathcal{L}_0(\theta_{\text{blz},i})}}. \quad (37)$$

In the next step, we can turn this equation into an expression for a marginalized χ^2 by using the definition of our likelihood ($\mathcal{L} = \exp(-\chi^2/2)$):

$$\begin{aligned} \Delta\bar{\chi}^2(\theta_{\text{DM}}) &= \bar{\chi}^2(\theta_{\text{DM}}) - \bar{\chi}_0^2 \\ &= -2 \log \frac{\sum_{i=1}^N \exp\left(-\frac{\chi^2(\theta_{\text{blz},i}, \theta_{\text{DM}}) - \chi_0^2(\theta_{\text{blz},i})}{2}\right)}{N}. \end{aligned} \quad (38)$$

Finally, we obtain the DM limit at the 95% confidence level from the requirement $\Delta\bar{\chi}^2(\theta_{\text{DM}}) \leq 3.84$.

In practice, we evaluate Equation (38) on a grid of m_{DM} , with 14 grid points logarithmically spaced between 10 GeV and 4 TeV. We note that the annihilation cross section $\langle\sigma_{\text{ann}}v\rangle$ only changes the normalization of the C_{P} contributions, but not the shape. The DM \times DM contribution scales with $\langle\sigma_{\text{ann}}v\rangle^2$, while the DM \times BLZ contribution scales linearly with $\langle\sigma_{\text{ann}}v\rangle$. So we can tabulate the C_{P} contributions of the background and DM at a reference value of $\langle\sigma_{\text{ann}}v\rangle = 3 \times 10^{-26} \text{ cm}^3/\text{s}$. The equal-weights set contains $\mathcal{O}(10^5)$ parameter vectors. After the tabulation, the evaluation of Equation (38) takes about one second. The importance sampling reduces the computing time by about a factor of 10, since the typical number of evaluations required for a full parameter scan of the blazar and DM parameters requires $\mathcal{O}(10^6)$ evaluations. A further advantage of the importance sampling is that the tabulation can be parallelized to an arbitrary degree, which is not possible for a Monte Carlo–based parameter sampling with MULTINEST.

3.4. Constraints on DM Annihilation

We derive the constraints on the annihilation of DM into a pair of $\bar{b}b$ quarks, which serve as an illustrative example. The limits for the other hadronic channels are expected to be at a similar level. The left panel of Figure 8 shows the marginalized $\Delta\bar{\chi}^2$ in the plane of the DM mass and the annihilation cross section, as derived from Equation (38). For DM masses between 15 and 140 GeV, a small DM contribution slightly improves the fit of the C_{P} data. However, it is statistically not significant. The maximal improvement of the $\Delta\bar{\chi}^2$ is ~ 3.5 , which corresponds to a local significance of less than 2σ and an even smaller global significance. Consequently, we can derive

the DM limits as a function of the DM mass. In the fiducial setup, namely, using the ‘‘LOW’’ model for the concentration–mass relation of the DM halos (see Section 3), we can place an upper limit of $\langle\sigma_{\text{ann}}v\rangle = 10^{-25} \text{ cm}^3 \text{ s}^{-1}$ on the annihilation cross section at the DM mass of 10 GeV. The limit gradually weakens to $\langle\sigma_{\text{ann}}v\rangle = 3 \times 10^{-23} \text{ cm}^3 \text{ s}^{-1}$ at 4 TeV. In a more aggressive setting for the concentration parameter, i.e., the ‘‘HIGH’’ model, we obtain a DM limit that is almost one order of magnitude stronger. The plot in the left panel of Figure 8 shows the limits for the ‘‘LOW’’ model, while the comparison between the two cases is shown in the right panel. In the ‘‘HIGH’’ scenario, we can exclude a thermal WIMP for $m_{\text{DM}} < 20 \text{ GeV}$.

As explained above, the measurement of the APS is dominated by the Poisson noise term. For this reason, the DM bounds in Figure 8 are weaker than the ones from other probes of the UGRB (Di Mauro & Donato 2015; Charles et al. 2016), such as the total intensity energy spectrum and the cross-correlation APS with gravitational tracers, which are less affected by the noise being linear instead of quadratic (see, e.g., Figure 4 in Regis et al. 2015). There are also other strategies of indirect DM searches using gamma rays, e.g., from the dwarf spheroidal galaxies or the Galactic center, or using cosmic-ray antiprotons. Those DM limits are typically stronger by 1–2 orders of magnitude (see, e.g., Leane 2020; Slatyer 2021 and references therein), but those analyses are affected by different systematic uncertainties.

In Figure 9, we show the contribution of all the different components to the C_{P} for two exemplary DM masses, of 100 GeV (left panel) and 1 TeV (right panel), in the ‘‘LOW’’ scenario. The DM components are evaluated at the $\langle\sigma_{\text{ann}}v\rangle$ values, corresponding to the limit shown in Figure 8 for that DM mass. As expected, the blazar components are dominant, and the DM only constitutes a subdominant part. The largest DM contribution stems from the extragalactic DM halos, closely followed by the contribution of Galactic DM subhalos, which is smaller roughly by a factor of 2, while the contribution of BLZ \times DM is smaller by 1–2 orders of magnitude. The uncertainty bands in Figure 9 represent the 1σ uncertainty in the blazar background models. In the ‘‘HIGH’’ scenario, the picture is similar, but with the DM contribution being strongly dominated by the extragalactic term.

Finally, we stress again that the absence of a DM signal in the C_{P} provides further confirmation that the sum of the FSRQs and BLLs fully explains the entire UGRB anisotropy, and that no additional weak component is required to match the data.

4. Conclusions

In this work, we compared models of the GLF and SED of blazars to the latest measurement of the energy spectrum of the UGRB anisotropies (Ackermann et al. 2018) and the properties of the resolved gamma-ray sources of the Fermi-LAT 4FGL catalog. We considered two different blazar populations, distinguishing between BLLs and FSRQs. We found that BLLs and FSRQs can account for the totality of the UGRB anisotropy, with BLLs dominating the APS at high energies, and FSRQs being important at GeV energies. The derived models well reproduce the size and spectral features observed by Ackermann et al. (2018) and the properties of the source number counts of the 4FGL catalog. Our analysis significantly constrains the redshift and luminosity dependence of the blazar GLF and the spectrum of the SED in the unresolved regime.

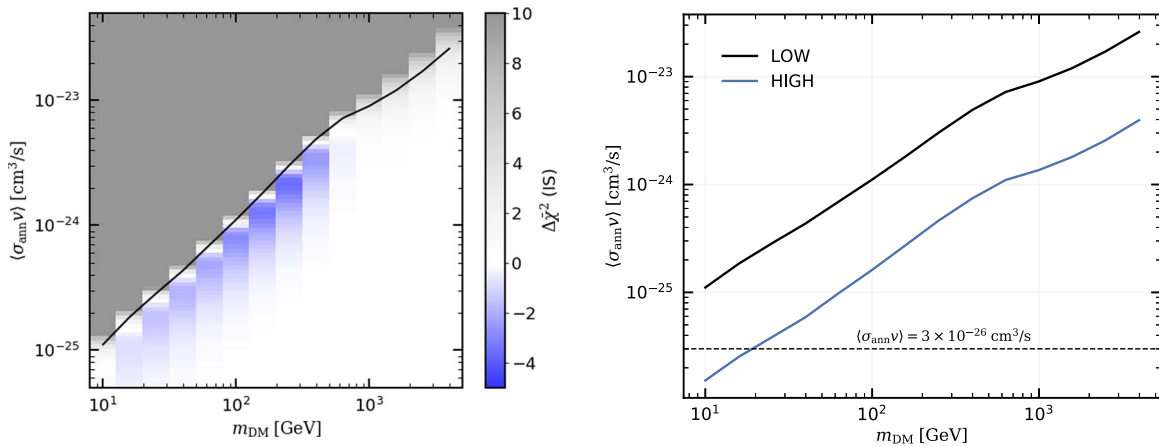


Figure 8. 95% confidence level bounds on the annihilation cross section as a function of the DM mass, for annihilation into $\bar{b}b$. The colors in the left panel stand for the value of the marginalized $\Delta\chi^2$ derived from Equation (38). The left panel shows the constraints in the “LOW” scenario, while the right panel reports the comparison between the “LOW” and “HIGH” cases.

We also calculate the contribution of the unresolved populations of FSRQs and BLLs to the UGRB intensity spectrum, finding a non-negligible contribution of about 30% between 10 and 100 GeV and about 20% at 1 GeV.

In the second part of the paper, we included a contribution to the UGRB arising from annihilating DM, and performed a global fit to derive constraints on the particle DM parameters. We computed both Galactic and extragalactic DM contributions, and included cross-terms in the APS, due to the cross-correlation of the blazars with the DM halos hosting them. The dominant term arises from extragalactic DM halos, and strongly depends on the poorly known description of DM subhalos. To bracket the uncertainty, we considered two different scenarios, “LOW” and “HIGH,” which lead to upper limits of $\langle\sigma_{\text{ann}}v\rangle = 10^{-25} \text{ cm}^3 \text{ s}^{-1}$ and $\langle\sigma_{\text{ann}}v\rangle = 1.5 \times 10^{-26} \text{ cm}^3 \text{ s}^{-1}$, respectively, on the annihilation cross section at the DM mass of 10 GeV, for annihilation into bottom quarks.

The present analysis of the UGRB anisotropies is based on the measurement of Ackermann et al. (2018), where no evidence for an ℓ -dependent APS was found. Further data, and more resolved sources, would allow us to reduce the level of the Poisson noise C_P and to measure an APS unveiling the large-scale clustering of gamma-ray sources. This would allow us to deepen our understanding of blazar populations, as well as exploit the APS observable in a much more powerful way in the context of DM bounds.

We thank S. Manconi for fruitful discussions throughout the work. Furthermore, we thank M. Di Mauro, T. Linden, and S. Manconi for helpful comments as well as careful reading of the manuscript. This work is supported by: the “Departments of Excellence 2018–2022” grant awarded by the Italian Ministry of Education, University and Research (MIUR) L. 232/2016; the research grant “The Anisotropic Dark Universe” No. CSTO161409, funded by Compagnia di San Paolo and the University of Turin; the research grant “TAsP (Theoretical Astroparticle Physics),” funded by INFN; the research grant “The Dark Universe: A Synergic Multimessenger Approach” No. 2017X7X85K, funded by MIUR; the research grants “Deciphering the high-energy sky via cross correlation” and “Unveiling dark matter and missing baryons in the high-energy sky,” funded by the agreement ASI-INAF n. 2017-14-H.0; and

the research grant “From Darklight to Dark Matter: understanding the galaxy/matter connection to measure the universe” No. 20179P3PKJ, funded by MIUR. M.N.: the material is based upon work supported by NASA, under award number 80GSFC21M0002. M.K. is partially supported by the Swedish National Space Agency, under contract 117/19, and the European Research Council, under grant 742104. E.P. is supported by the Fermi Research Alliance, LLC, under Contract No. DE-AC02-07CH11359, with the U.S. Department of Energy, Office of High Energy Physics. Computations were enabled by resources provided by the Swedish National Infrastructure for Computing (SNIC), under the project No. 2020/5-463, partially funded by the Swedish Research Council through grant agreement no. 2018-05973. Furthermore, some computations in this work were performed with computing resources granted by RWTH Aachen University, under project No. rwth0578.

Appendix A One or Two Populations: A Phenomenological Interpretation

In this paper, we have considered two blazar populations, BLLs and FSRQs. Both populations are important, and their sum provides a good fit to angular correlations of the UGRB. In more detail, FSRQs provide the largest contributions to the C_P below a few GeV, while BLLs dominate at higher energies. As a consequence, we found that FSRQs are responsible for the softening of the C_P at low energies, which is an interesting result, because this softening has also been interpreted as a possible hint of a new source population (Ando et al. 2017). In a similar spirit, Ackermann et al. (2018) also claimed that the C_P data hints at two populations. On the other hand, in Manconi et al. (2020), a good fit of the C_P data is obtained with one population, using a model that combines FSRQs and BLLs into a single GLF and SED model.

Here, we explore the issue of one versus two populations more thoroughly, by employing a phenomenological model for the SED and GLF of two hypothetical source populations. The phenomenological model is slightly simplified as compared to the physical models for the GLFs and SEDs of the BLL and FSRQ source populations used in the main text. The most important difference is that the phenomenological model does not include a redshift dependence. However, the C_P data is not

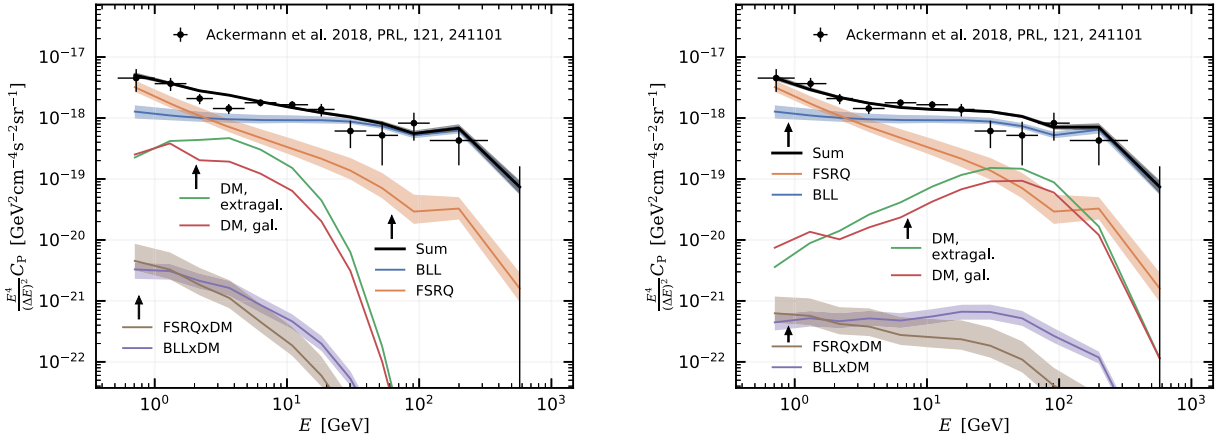


Figure 9. Comparison of the C_p from blazars and DM. The DM contribution is shown at 100 GeV (left) and 1 TeV (right), and computed in the “LOW” scenario, for annihilation into $\bar{b}b$. In both panels, we choose a value of $\langle\sigma_{\text{ann}}v\rangle$ of DM at the limit derived in Figure 8.

sensitive to redshift information, because it is integrated along the line of sight. We find that our model is sufficient to explore the question regarding the number of source populations. Furthermore, it has the clear advantage that large parts of the computations can be done analytically. We find that the width of the spectral index distribution is a key parameter for distinguishing the scenarios of one or two populations.

A.1. Definition of the GLF and SED

The source count distribution as a function of the photon flux S is modeled as a power law:

$$\frac{dN}{dS} = A \left(\frac{S}{S_0} \right)^{-\gamma}, \quad (\text{A1})$$

where A is an overall normalization, γ is the power-law index, and S_0 is a reference flux. In the following, S_0 is fixed to $1 \times 10^{-10} \text{ cm}^2 \text{ s}^{-1}$, and the fluxes S and S_0 always refer to the photon flux in the energy bin from 1 to 100 GeV. To relate the flux S to the flux S_i in a different energy bin i , we need the SED, which we model as a power law with an exponential cutoff:

$$\frac{dN}{dE} = K \left(\frac{E}{E_0} \right)^{-\Gamma} \exp\left(-\frac{E}{E_c}\right). \quad (\text{A2})$$

Here, K is the normalization, E_0 is a reference energy, Γ is the photon spectral index, and E_c is the energy of the exponential cutoff. The exponential cutoff allows the mimicking of the attenuation of gamma rays at high energies. By definition, the flux S is given by $S = \int_{1 \text{ GeV}}^{100 \text{ GeV}} dE dN/dE$. So the ratio of the fluxes S_i and S is given by:

$$s_i = \frac{S_i}{S} = \frac{\int_{E_{\text{min},i}}^{E_{\text{max},i}} dE E^{-\Gamma} \exp(-E/E_c)}{\int_{1 \text{ GeV}}^{100 \text{ GeV}} dE E^{-\Gamma} \exp(-E/E_c)}. \quad (\text{A3})$$

Finally, we allow for an intrinsic distribution of the photon spectral indices, following a Gaussian with mean μ and width

σ :

$$\frac{dN}{d\Gamma} = \frac{1}{\sqrt{2\pi}\sigma} \exp\left(-\frac{(\mu - \Gamma)^2}{2\sigma^2}\right). \quad (\text{A4})$$

Then the C_p of the unresolved point sources is given by

$$C_p^{ij} = \int dS d\Gamma S_i S_j \frac{d^2 N}{dS d\Gamma} [1 - \Omega(S, \Gamma)], \quad (\text{A5})$$

where $\Omega(S, \Gamma)$ is the detector efficiency for resolving point sources, which we model as a θ -function at a Γ -dependent flux threshold, S_{thr} (see the main text). By considering photon spectral indices between 1 and 3, the C_p is then calculated as

$$\begin{aligned} C_p^{ij} &= \int_1^3 d\Gamma \int_0^{S_{\text{thr}}(\Gamma)} dS \frac{1}{\sqrt{2\pi}\sigma} \exp\left(-\frac{(\mu - \Gamma)^2}{2\sigma^2}\right) \\ &\quad \times S^2 s_i s_j A \left(\frac{S}{S_0} \right)^{-\gamma} \\ &= \int_1^3 d\Gamma \frac{1}{\sqrt{2\pi}\sigma} \exp\left(-\frac{(\mu - \Gamma)^2}{2\sigma^2}\right) \\ &\quad \times s_i s_j \frac{A S_{\text{thr}}^3(\Gamma)}{3 - \gamma} \left(\frac{S_{\text{thr}}(\Gamma)}{S_0} \right)^{-\gamma}. \end{aligned} \quad (\text{A6})$$

We note that all the energy information of the C_p is encoded in the factor $s_i s_j$, such that, to a first approximation, the slope, γ , of the dN/dS is degenerate with the overall normalization, A . So we fix γ to a benchmark value of 2.2 in the following analysis.

A.2. Fits and Results for the Phenomenological Model

In this section, we perform a total of four fits. The fits differ by the number of source populations (one or two) and by the inclusion of a distribution in the photon spectral index.

In the first two fits, we neglect the distribution of spectral indices—namely, we force $\sigma = 0$. The first analysis then employs a single source population, with the SED and GLF as specified in the previous section. The free parameters are the normalization of the GLF (A), the photon spectral index (μ), and the energy cutoff of the SED (E_c). Furthermore, we use a nuisance parameter (k_{C_p}) that varies the value of the flux threshold (see the main text for more details). This fit has four free parameters. In the second analysis, we use two source

Table 3
Fit Results of the Phenomenological Model

	w/o Γ Distribution			w/ Γ Distribution		
	1 pop.	2 pops		1 pop.	2 pops	
		pop. a	pop. b		pop. a	pop. b
$\log_{10}(A [\text{cm}^{-2}\text{s}^{-1}\text{sr}])$	$12.18^{+0.17}_{-0.16}$	$11.87^{+0.36}_{-0.13}$	$11.88^{+0.34}_{-0.17}$	$12.26^{+0.15}_{-0.18}$	$11.71^{+0.81}_{-0.20}$	$11.52^{+0.96}_{-0.42}$
μ	$2.11^{+0.04}_{-0.03}$	$1.86^{+0.19}_{-0.11}$	$2.50^{+0.18}_{-0.29}$	$2.18^{+0.06}_{-0.05}$	$2.02^{+0.22}_{-0.07}$	$2.44^{+0.17}_{-0.32}$
σ	$0.34^{+0.07}_{-0.08}$	$0.30^{+0.13}_{-0.09}$	$0.30^{+0.18}_{-0.08}$
$\log_{10}(E_c [\text{GeV}])$	$2.19^{+0.12}_{-0.13}$	$1.98^{+0.12}_{-0.15}$		$1.88^{+0.10}_{-0.12}$	$1.88^{+0.10}_{-0.11}$	
k_{Cp}	$1.00^{+0.29}_{-0.50}$	$1.00^{+0.29}_{-0.50}$		$1.00^{+0.96}_{-0.24}$	$0.97^{+0.38}_{-0.42}$	
χ^2	85.2	74.9		74.7	74.5	
$\Delta\chi^2$		10.3			0.2	

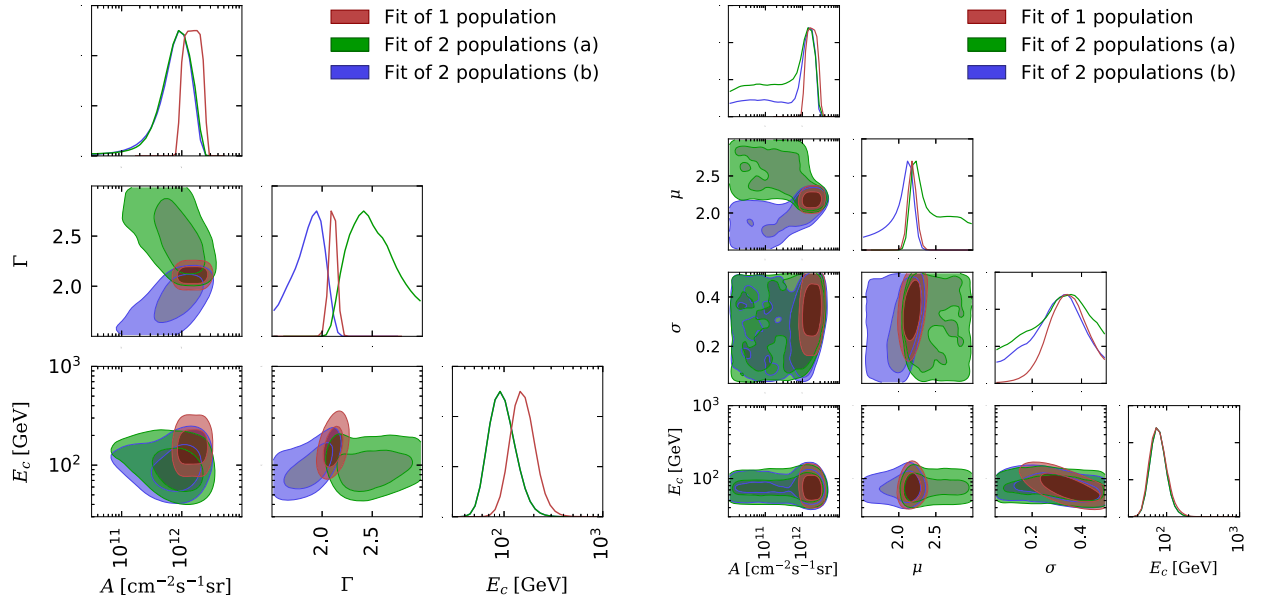


Figure 10. Triangle plots showing the best-fit region of the phenomenological model fitted to the C_p data for the different fit setups. On the diagonal, we display the marginalized likelihood for all parameters, and the remaining panels below the diagonal contain the 1σ and 2σ contours derived from the marginalized likelihood in two dimensions for each parameter combination. The red contours and lines correspond to a fit with a single population, while the green and blue contours correspond to the two different populations of the fit containing two populations (labeled “a” and “b”). Left panel: the phenomenological model with a fixed photon spectral index. Right panel: the phenomenological model with a Gaussian distribution of the photon spectral index.

populations, labeled a and b . They have the same functional form, but different parameters: in particular, for the normalization of the GLF and the photon spectral index. However, we force them to have the same value for the cutoff, E_c . Together with the nuisance parameter, this amounts to six free parameters. To avoid an extra degeneracy in the fit, we restrict the photon spectral indices to $\mu_a < \mu_b$.

The third and fourth fits are very similar to the first two, but we allow for a distribution in Γ . Consequently, this leads to one (σ) and two (σ_a and σ_b) more parameters in the fits, respectively. We use the MULTINEST code to perform the four fits and to obtain the posterior distributions presented in the following. The uncertainties are stated in the Bayesian statistical framework.

The results of our four fits are presented in Table 3 and Figure 10. The $\chi^2/\text{degrees of freedom}$ of all four fits are close to 1, and we conclude that all of them give a good fit to the C_p data. However, when comparing the χ^2 's of the first and second fits, i.e., the fits without the Γ distribution, we see that including a second population reduces the total χ^2 by 10.3, which formally corresponds to a statistical shift by 2.8σ . So this

could be interpreted as a small hint of two populations. However, if we look at the results with a Γ distribution, the conclusion changes. Here, the χ^2 only decreases by 0.2 when a second population is introduced, which is not significant. So we cannot distinguish between one or two populations based only on the C_p data. This can also be seen from the triangle plots in Figure 10. Without allowing for a Γ distribution, the red posterior contours (one population) are not fully included in either the green or blue contours (population a or b of the two-population fit). Furthermore, both populations, a and b , are required to have a relatively high normalization of $A > 10^{-11} \text{cm}^{-2} \text{s}^{-1} \text{sr}^{-1}$. On the other hand, if we allow for a Γ distribution, the red contours are fully included in both the green and blue contours. And, in the case of two populations, one of the normalizations A can be pushed to negligible values of $10^{-12} \text{cm}^{-2} \text{s}^{-1} \text{sr}^{-1}$. We compare the C_p energy autocorrelations of the best fit to the data in Figure 11. It is clearly visible that, in the case without the Γ distribution, two populations provide a better fit, while in the case with the Γ distribution there is almost no difference.

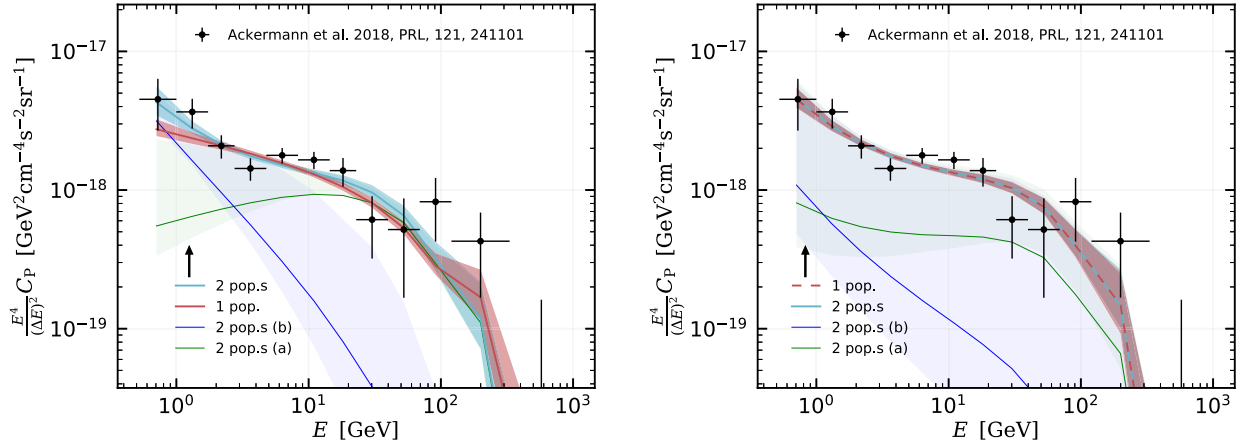


Figure 11. Left panel: the phenomenological model with a fixed photon spectral index. Right panel: the phenomenological model with a Gaussian distribution of the photon spectral index.

Finally, we have a look at the C_P energy correlation matrix (the coefficients are defined as $C_P^{ij} / \sqrt{C_P^{ii} C_P^{jj}}$). By definition, the diagonal coefficients are equal to one. If there was only one source population with a single and fixed photon spectral index, the offdiagonal coefficients would also be equal to 1. Instead, the C_P measurement (Ackermann et al. 2018) showed that the offdiagonal coefficients are ~ 0.6 , which was interpreted as an indication of two populations. In Figure 12, we also show that a single source population with a distribution of photon spectral indices provides the correct offdiagonal pattern.

A.3. Conclusions

We conclude that, based on the C_P measurement itself, it is not possible to distinguish between two populations with narrow spectral index distributions and a single population with a broader distribution. In the latter case, the required value for the width of the Γ distribution is $\sigma = 0.34^{+0.07}_{-0.08}$. Additional information can help to solve the riddle. In the analysis of the main text, we included a physical model and the constraining power from the 4FGL catalog. This allowed us to break the degeneracy and to determine the presence of two populations, BLLs and FSRQs.

Appendix B Calculation of the Bayes Factor

In the main text, we use a physical model with two populations, BLLs and FSRQs. Because of the 4FGL catalog prior, this model is significantly preferred over a model with only one BLL population. This can be quantified by the calculation of the Bayes factor, which is briefly summarized here. The Bayes factor is defined as the ratio of evidence between the two hypotheses: two populations (labeled “all”) and one population (labeled “BLL”). For flat priors, this becomes

$$B = \frac{Z_{\text{all}}}{Z_{\text{BLL}}} = \frac{\int d\theta_{\text{blz}} \mathcal{L}_{4\text{FGL}}(\theta_{\text{blz}}) \mathcal{L}_{C_P, \text{all}}(\theta_{\text{blz}})}{\int d\theta_{\text{blz}} \mathcal{L}_{4\text{FGL}}(\theta_{\text{blz}}) \mathcal{L}_{C_P, \text{BLL}}(\theta_{\text{BLL}})}. \quad (\text{B1})$$

Here, $\mathcal{L}_{C_P, \text{all}}$ and $\mathcal{L}_{C_P, \text{BLL}}$ are the likelihoods for the C_P data using the sum of BLLs plus FSRQs and only BLLs, respectively. We note that the C_P likelihoods also depend on the nuisance parameters θ_n , which we suppress in the notation.

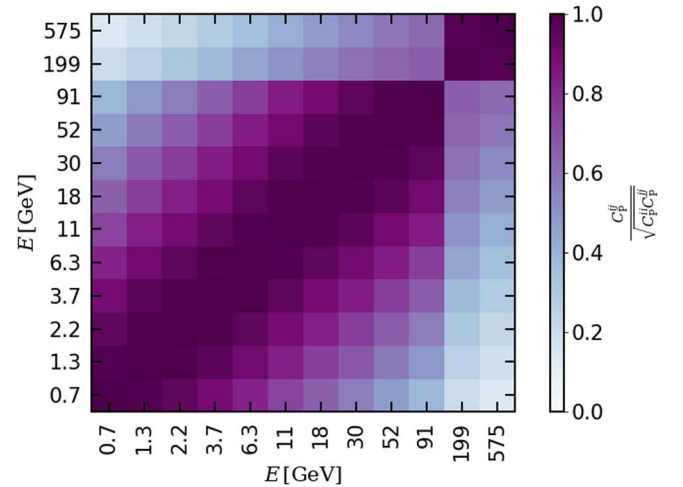


Figure 12. The C_P energy correlation matrix for the phenomenological model in the setup with only one population, but including a Γ distribution.

In analogy to Equation (34), we can approximately replace the integrals by sums,

$$B \approx \frac{\sum_i \mathcal{L}_{C_P, \text{all}}(\theta_{\text{blz}, i})}{\sum_i \mathcal{L}_{C_P, \text{BLL}}(\theta_{\text{BLL}, i})}, \quad (\text{B2})$$

where i runs over all the points in the equal-weights sample of the 4FGL-only fit. Finally, we note one subtlety: the normalization of the C_P model strongly depends on the exact value of the catalog threshold, which is only known approximately. To take the uncertainty due to the threshold into account, we profile over the C_P normalization, individually for each parameter point i . The mean renormalization factors are 1.04 and 1.16 for the hypotheses of two populations and one population, respectively.

Appendix C Resolving Previous UGRB Anisotropy Measurements

As mentioned in the main text, the UGRB emission is exposure-dependent: the more the LAT observes, the more sensitive is the survey to fainter sources, and consequently less unresolved emission contributes to the UGRB. We show this effect by comparing the UGRB anisotropy energy spectrum measured by Fornasa et al. (2016), which masked sources from

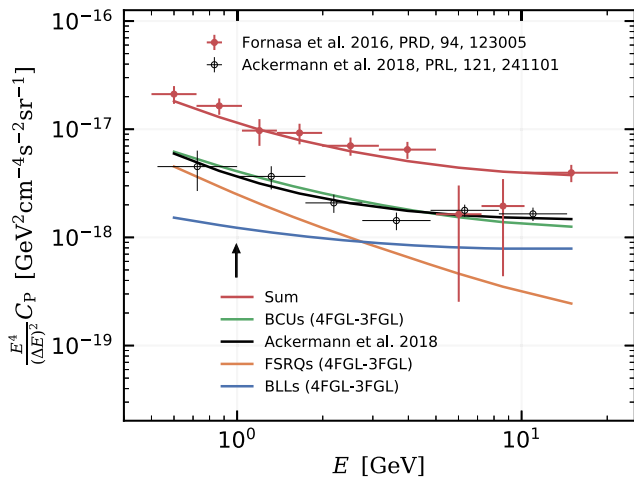


Figure 13. Comparison between the measurements from Fornasa et al. (2016; red points) and Ackermann et al. (2018; black points). The C_p s of the populations of FSRQs, BLLs, and BCUs of the 4FGL that are not yet resolved in the 3FGL are shown in orange, blue, and green, respectively, and the best fit to the C_p of Ackermann et al. (2018) is given by the black curve. Their sum is shown with the red curve, which well reproduces the measurement of Fornasa et al. (2016). The comparison is restricted to energies below 10 GeV (see the text).

the 3FGL source catalog (Acero et al. 2015), based on 4 yr of the LAT survey, with the one in Ackermann et al. (2018). In Figure 13, we report both measurements in red and black, respectively. The difference between the two measurements, which consider similar total mission times (7.5 yr in Fornasa et al. 2016 and 8 yr in Ackermann et al. 2018), is mainly due to the difference in the number of resolved sources masked away from the analyzed maps: the 4FGL counts approximately 2000 more sources than the 3FGL. We test this by evaluating the anisotropy energy spectrum of the populations of FSRQs, BLLs, and BCUs of the 4FGL that are not yet resolved (i.e., not present) in the 3FGL (let us call this $\Delta C_{p,4FGL-3FGL}$). We verify that the sum of the best-fit model of the measurement in Ackermann et al. (2018) plus the $\Delta C_{p,4FGL-3FGL}$ reproduces the anisotropy energy spectrum as measured by Fornasa et al. (2016). In agreement with our expectations, the results in Figure 13 show that there is a transition between FSRQs and BLLs in the $\Delta C_{p,4FGL-3FGL}$ when going from lower to higher energies. So it is plausible to observe a similar transition in the C_p measurement of Ackermann et al. (2018).

This test is performed by only considering energies up to 10 GeV. The measurement by Ackermann et al. (2018) also masks 3FHL sources above those energies, making the comparison with Fornasa et al. (2016) less straightforward and beyond the scope of this study.

ORCID iDs

Michael Korsmeier  <https://orcid.org/0000-0003-3478-888X>

Elena Pinetti  <https://orcid.org/0000-0001-7070-0094>
 Michela Negro  <https://orcid.org/0000-0002-6548-5622>
 Marco Regis  <https://orcid.org/0000-0003-0399-0284>
 Nicolao Fornengo  <https://orcid.org/0000-0002-3074-3118>

References

- Abdo, A. A., Ackermann, M., Ajello, M., et al. 2010, *PhRl*, 104, 101101
 Abdollahi, S., Acero, F., Ackermann, M., et al. 2020, *ApJ*, 247, 33
 Acero, F., Ackermann, M., Ajello, M., et al. 2015, *ApJS*, 218, 23
 Ackermann, M., Ajello, M., Albert, A., et al. 2012, *PhRvD*, 85, 083007
 Ackermann, M., Ajello, A., Albert, A., et al. 2015, *ApJ*, 799, 86
 Ackermann, M., Ajello, M., Atwood, W. B., et al. 2015, *ApJ*, 810, 14
 Ackermann, M., Ajello, M., Baldini, L., et al. 2018, *PhRvL*, 121, 241101
 Aghanim, N., Akrami, Y., Ashdown, M., et al. 2020, *A&A*, 641, A6
 Ajello, M., Gasparri, D., Sánchez-Conde, M., et al. 2015, *AJ*, 800, L27
 Ajello, M., Shaw, M. S., Romani, R. W., et al. 2012, *ApJ*, 751, 108
 Ajello, M., Romani, R. W., Gasparri, D., et al. 2014, *ApJ*, 780, 73
 Ajello, M., Angioni, R., Axelsson, M., et al. 2020, *ApJ*, 892, 105
 Ammazzalorso, S., Gruen, D., Regis, M., et al. 2020, *PhRvL*, 124, 101102
 Ando, S. 2009, *PhRv*, D80, 023520
 Ando, S., Fornasa, M., Fornengo, N., Regis, M., & Zechlin, H.-S. 2017, *PhRv*, D95, 123006
 Ando, S., & Komatsu, E. 2006, *PhRvD*, 73, 023521
 Atwood, W. B., Abdo, A. A., Ackermann, M., et al. 2009, *ApJ*, 697, 1071
 Bringmann, T., Calore, F., Di Mauro, M., & Donato, F. 2014, *PhRv*, D89, 023012
 Camera, S., Fornasa, M., Fornengo, N., & Regis, M. 2015, *JCAP*, 1506, 029
 Charles, E., Sánchez-Conde, M., Anderson, B., et al. 2016, *PhR*, 636, 1
 Cooray, A., & Sheth, R. 2002, *PhR*, 372, 1
 Correa, C. A., Wyithe, J. S. B., Schaye, J., & Duffy, A. R. 2015, *MNRAS*, 452, 1217
 Cuoco, A., Komatsu, E., & Siegal-Gaskins, J. M. 2012, *PhRvD*, 86, 063004
 Cuoco, A., Xia, J.-Q., Regis, M., et al. 2015, *ApJS*, 221, 29
 Di Mauro, M., Calore, F., Donato, F., Ajello, M., & Latronico, L. 2013, *ApJ*, 780, 161
 Di Mauro, M., Cuoco, A., Donato, F., & Siegal-Gaskins, J. M. 2014, *JCAP*, 2014, 021
 Di Mauro, M., & Donato, F. 2015, *PhRv*, D91, 123001
 Di Mauro, M., Manconi, S., Zechlin, H. S., et al. 2018, *ApJ*, 856, 106
 Feroz, F., Hobson, M. P., & Bridges, M. 2009, *MNRAS*, 398, 1601
 Finke, J. D., Razzaque, S., & Dermer, C. D. 2010, *ApJ*, 712, 238
 Fornasa, M., & Sánchez-Conde, M. A. 2015, *PhR*, 598, 1
 Fornasa, M., Cuoco, A., Zavala, J., et al. 2016, *PhRv*, D94, 123005
 Fornengo, N., & Regis, M. 2014, *FrP*, 2, 6
 Kahlhoefer, F., Korsmeier, M., Krämer, M., Manconi, S., & Nippel, K. 2021, *JCAP*, 12, 037
 Leane, R. K. 2020, arXiv:2006.00513
 Lisanti, M., Mishra-Sharma, S., Necib, L., & Safdi, B. R. 2016, *ApJ*, 832, 117
 Manconi, S., Korsmeier, M., Donato, F., et al. 2020, *PhRvD*, 101, 103026
 Navarro, J. F., Frenk, C. S., & White, S. D. M. 1996, *ApJ*, 462, 563
 Neto, A. F., Gao, L., Bett, P., et al. 2007, *MNRAS*, 381, 1450
 Nolan, P. L., Abdo, A. A., Ackermann, M., et al. 2012, *ApJS*, 199, 31
 Regis, M., Xia, J.-Q., Cuoco, A., et al. 2015, *PhRvL*, 114, 241301
 Roth, M. A., Krumholz, M. R., Crocker, R. M., & Celli, S. 2021, *Natur*, 597, 341
 Slatyer, T. R. 2021, arXiv:2109.02696
 Tamborra, I., Ando, S., & Murase, K. 2014, *JCAP*, 9, 043
 Zechlin, H.-S., Cuoco, A., Donato, F., Fornengo, N., & Regis, M. 2016a, *ApJL*, 826, L31
 Zechlin, H.-S., Cuoco, A., Donato, F., Fornengo, N., & Vittino, A. 2016b, *ApJS*, 225, 18
 Zechlin, H.-S., Manconi, S., & Donato, F. 2018, *PhRv*, D98, 083022